Deformation-related volcanism in the Pacific Ocean linked to the Hawaiian-Emperor bend

John M. O'Connor[1,2,3], Kaj Hoernle[4], R. Dietmar Müller[5], Jason P. Morgan[6,] Nathaniel P. Butterworth[5], Folkmar Hauff[4], David T. Sandwell[7], Wilfried Jokat[1], Jan R. Wijbrans[3], Peter Stoffers[8]

[1]Alfred Wegener Institute for Polar and Marine Research, Bremerhaven, Germany
[2]GeoZentrum Nordbayern, University Erlangen-Nürnberg, Germany
[3]Faculty of Earth and Life Sciences, VU University Amsterdam, The Netherlands
[4]GEOMAR Helmholtz Centre for Ocean Research Kiel, Germany
[5]EarthByte Group, School of Geosciences, The University of Sydney, New South Wales, Australia
[6] Royal Holloway, University of London, UK
[7]Scripps Institution of Oceanography, La Jolla, California, USA
[8]Institute for Geosciences, Christian-Albrechts-University, Kiel, Germany

Preprint submitted to Nature Geoscience. March 2015

Despite the overall success of the mantle plume paradigm, it has become increasingly clear that not all seamounts and volcanic ridges on the Pacific Ocean floor owe their origin to hotspots[1]. Some might be caused by cracks in the ocean crust linked to plate reorganisations[1-3]. Explanations for the Hawaiian-Emperor Bend (HEB) vary from changes in the direction of the Pacific plate[4,5], motion of the Hawaiian hotspot[6-8], to a combination of both[9]. These alternative plate motion and mantle mechanisms have important implications for understanding global plate motion, mantle convection and mantle plumes[6,7,10,11]. Linking the HEB with plate reorganisation has long been uncertain, because there is no independent record that precisely dates tectonic events affecting the Pacific plate. Here we use age and geochemical evidence from unusual seafloor volcanism, which is more similar to mid-ocean ridge than ocean island volcanism, to infer a link between the HEB and a series of subduction events that started 53-52 Ma ago, and continued to c. 47 Ma. Our results indicate that the HEB is linked to subduction initiation events, which may have changed asthenosphere flow and the shallow motion of the Hawaiian plume in addition to plate motion.

Both changes in mantle flow[6-8] and in the direction of Pacific plate motion[4,5] have been proposed to explain the HEB. Decreasing paleolatitudes during the formation of the Emperor Seamounts[6,8], and combined global mantle flow and plate motion models[5], support mantle flow as the dominant mechanism for creating the HEB. A paleomagnetic pole for the Pacific plate (based on the skewness of vector aeromagnetic profiles of magnetic anomalies due to seafloor spreading) has been interpreted as evidence that 5 ± 3° of the southward motion of the Hawaiian hotspot occurred after 32 Ma[12], thus post-dating the formation of the Emperor seamounts, but the robustness of this type of analysis has been questioned (Supplementary Note 1). An alternative hypothesis notes the broad coincidence of the HEB with major circum-Pacific plate tectonic events and favours HEB formation by the resulting change in the direction of Pacific plate motion[4,5,10,13]. But plate reconstructions connecting the Indo-Atlantic realm to the Pacific for Late Cretaceous predict a negligible bend[11].

While diverse lines of evidence record a rough correlation between other circum-Pacific tectonic changes (Supplementary Note 2) and formation of the HEB[5,10,14], their timing has been too drawn-out to establish a connection. Here we report the unexpected discovery of the long-sought-after independent temporal record of circum-Pacific tectonic events while investigating a new type of linear structure on the Pacific

seafloor detected in recent years by improvements in satellite altimetry[2]. This new type of structure consists of groups of linear *en échelon* volcanic ridges, first described in 1987 for the 'Crossgrain' ridges located in the central Pacific[2]. Mechanisms explaining these linear ridge groups include hotspot-spreading ridge interaction[15] and tensional cracking of the Pacific plate[2,3] (see Supplementary Note 3).

In order to investigate the origin of these enigmatic structures, we carried out seismic surveys and dredge sampled the *en échelon* linear ridges, extending eastward in clusters, from the northern and southern ends of the Musicians Seamount Chain and the Murray Fracture Zone (FZ) on RV *Sonne* cruise SO142 (Fig. 1 and Supplementary Fig. 1 and Supplementary Table 1). The Musicians seamounts form a NW trending age-progressive Cretaceous hotspot track, located several hundred kilometres northwest of the Hawaiian Seamounts, best explained by plate motion over a now extinct Musicians hotspot[15,16]. The cluster of ridges extending from the southern end of the Musicians seamount chain is bounded to the north by the Murray FZ, which consists of a ~100 km band of linear ridges and troughs that stretch from the Musicians to the Hawaiian Seamount Chain[16]. We dredge sampled one of these volcanic ridges in the Murray FZ (Fig. 1).

Seismic profiles collected during the SO142 expedition show that the Musicians ridges were formed by volcanism[15]. The volcanism is interpreted to have been generated by flow of mantle along channels in the base of the lithosphere from the Musicians hotspot to the Pacific-Farallon spreading centre in the Cretaceous[15]. While this is consistent with the ~94 – 92 Ma $^{40}Ar/^{39}Ar$ ages for two samples dredged from the volcanic ridge located furthest away from the northern end of the Musicians Chain (Fig. 1), most of the $^{40}Ar/^{39}Ar$ ages for the southern Musicians Ridges are unexpectedly 52-53 Ma. A few younger ages show that volcanism might have continued until 47-48 Ma, or that a second event occurred roughly 6 Ma later. Surprisingly, the samples from the Murray FZ also yielded ages of 47-48 Ma. $^{40}Ar/^{39}Ar$ plateau ages are in Fig. 2 and Supplementary Fig. 2. For complete information see Supplementary Table 2 and Methods and Supplementary Methods. The most striking facet of these unexpectedly young lava ages is they bracket the formation of the HEB (50-47 Ma)[5,9] (see also Supplementary Fig. 3).

The geochemistry of this late-stage volcanism can help constrain its origin (Fig. 3 and Supplementary Fig. 4 and Supplementary Table 2). The dated samples are unlike rejuvenated (or post-erosional) volcanism found on intraplate volcanoes, such as the

Hawaiian Island volcanoes, because they are tholeiitic and are depleted in both incompatible element and isotopic composition, whereas rejuvenated volcanism is alkalic and shows incompatible element enrichment (see also Supplementary Note 4). The late-stage Musicians lavas have similar major and trace element and Sr-Nd-Pb isotopic compositions to mid-ocean ridge basalts (MORB), consistent with their derivation from shallow upper mantle sources, despite not having been formed at a mid-ocean ridge.

The best and most obvious explanation for this new type of MORB-like, non-hotspot intraplate volcanism is that it records increased plate deformation that caused magmatism through decompression melting with plate cracking (reactivation of Cretaceous linear features) possibly facilitating and focussing magma ascent[e.g. 2,3]. Some possible present-day analogs for the type of deformation and volcanism that we invoke here for the early Tertiary are the *en échelon* ridges in the extensional part of the Capricorn-Australia plate boundary[17], as well as the Pukapuka ridges in the central Pacific[18]. Another analogue might be located to the west of the Mid-Atlantic Ridge, where the Researcher volcanic ridge and graben system to the north form an *en échelon* volcano-tectonic complex that is extensional in character (Supplementary Note 5).

There is evidence also in the geologic record to show that subduction forces can cause plate yielding[19] (Supplementary Note 6). For example, there is extensive geological evidence indicating that subduction initiation along the western Pacific caused the tectonic events surrounding the Pacific, and led to the onset of uplift of the Transantarctic Mountains (Supplementary Note 2). It seems reasonable, therefore, to infer from the striking synchronicity between the 53-52 Ma tectonic-magmatic event and subduction of the Izanagi-Pacific spreading ridge ~52-51 Ma[10,20], and subduction initiation at the IBM and Tonga ~51.5 Ma (as measured by subduction related volcanism)[19,21-23], that they might be causally connected (Fig. 4). Moreover, the initiation of Aleutian subduction at end of this subduction zone reorganisation[24,25], coincides with the observed 47-48 Ma magmatism.

If increased stress within the plate was the sole mechanism controlling the location and timing of this new style of MORB-like intraplate volcanism, then it is likely to be distributed widely across the Pacific seafloor. Since relatively few intraplate structures in the Pacific have been sampled and dated, we do not know if there is evidence for widespread deformation-related volcanism between 52-53 and 47-48 Ma. Nevertheless, local plate and shallow mantle melting and flow anomalies are likely to determine

where MORB-like intraplate volcanism occurs during intervals of increased plate stress (see Supplementary Note 3).

Current numerical models of the subduction-related forces driving the Pacific plate do not incorporate local plate and mantle anomalies and so cannot predict where and when plate cracking and decompression melting might trigger intraplate volcanism across the Pacific plate. Numerical modelling, however, does point to the possibility that a major plate-wide change in subduction topology between 62 and 52 Ma might have led to an increase in plate speed and intraplate deformation across the Pacific plate[26].

A possible plate-scale mechanism for changing asthenospheric flow might be a gradual westward speed-up of the Farallon-Pacific spreading rates, possibly starting at ~50 Ma, which was caused by the increasing pull on the Pacific Plate exerted by the subducting slabs in the IBM and Tonga subduction zones[20,26]. This timing corresponds to the part of the Hawaiian-Emperor Seamount Chain where the trend first starts to rotate from nearly due south to east-southeast, just north of Daikakuji and near Kimmei seamount, marking the time of inception of the HEB ≥50 Ma and not the most arcuate 47.5 Ma part on the bend[5,9] (see also Supplementary Fig. 3).

Increasing pull from the IBM and Tonga subducing slabs could have caused Pacific plate speed-up at ~50 Ma[20,26] and might have gradually changed the resistance or dragging force associated with the interface between the upper mantle and plate (basal drag or basal shear force), which is usually considered to act in an opposite direction to absolute motion[27]. As the plate accelerated to the northwest asthenosphere counterflow could have increased in the opposite direction, deflecting the Hawaiian plume to the southeast during its final ascent through the transition zone[28] reflected in the change in the trend of the Emperor Chain at Kimmei seamount.

A change in asthenosphere flow at ~50 Ma might also have initiated the start of final plume slowdown[9] before the sharp 47.5 Ma HEB. This shallow mantle mechanism would fit with an explanation for plume motion and slowdown involving a capture and release mechanism, which also involves plate processes in the form of waning Kula-Pacific spreading[11]. A further change in the basal drag force might have resulted from initiation of subduction to the north in the Aleutians at the time of the sharp HEB.

In summary, the apparent reactivation of the Cretaceous Musicians Ridges started at the same time as a series of major inter-connected subduction events around the

Pacific margins. Local factors, such as lithospheric age and structure[e.g. 2,3,18], possibly by operating in combination with other types of secondary small scale sub-lithospheric convection[29], no doubt influenced the location of late-stage, MORB-like intraplate volcanism. For example, the ~75 Ma and ~57 Ma HE-type bends in the Gilberts and Tokelau seamount chains are linked to reactivation of preconditioned lithosphere by jerk-like plate extensions in the Pacific plate[30]. The HEB began at ≥50 Ma[5,9], when pull from these subducting slabs was sufficient to change Pacific plate motion, which we infer could have triggered a change in asthenospheric flow.

In conclusion, based on the timing and geochemistry of an unusual MORB-type of intraplate volcanism, we propose that subduction initiation events along the western and northern Pacific, respectively, caused internal plate deformation that might have triggered magmatism due to decompression melting, possibly associated with cracking of the upper oceanic plate and other local plate and shallow mantle mechanisms. We infer that the HEB morphology and a slowdown in posited plume motion correlate with changes in asthenosphere flow resulting from plate speed-up caused by increasing pull on the Pacific plate following subduction of the Izanagi-Pacific Ridge and initiation of Aleutian subduction. Thus, the HEB might be linked to subduction driven asthenospheric changes at a time when the rapidly moving Hawaiian plume was slowing down. Such a model is compatible with current estimates of plume motion based on drill-site paleolatitude information[6] and could be further tested with new very deep drill sites, because only with these will there be any hope of constraining changes of motion within the overall southward drift.

This new style of non-hotspot-related intraplate volcanic reactivation represents a potentially powerful new proxy for identifying and dating intraplate deformation caused by plate reorganisation events. Depending on the scale of asthenosphere changes, deflection and smearing out of plumes in the shallow mantle related to such events might correlate with regional or plate wide changes in the motion and volume flux of hotspot tracks, and account for at least some of the non-age progressive' intraplate volcanism widely found across the Pacific[1].

Methods

The ArArCALC $^{40}Ar/^{39}Ar$ age data files in Microsoft Excel format are provided in the Supplementary Information. The ArArCALC v2.5 software and detailed information are available at http://earthref.org/ArArCALC/. Further details are outlined in the Supplementary Methods.

References

1. Koppers, A. A. P. Mantle plumes persevere. *Nature Geoscience* **4**, 816–817 (2011).
2. Winterer, E. L., & Sandwell, D. T. Evidence from en-echelon cross-grain ridges for tensional cracks in the Pacific plate. *Nature* **329**, 534-537 (1987).
3. Natland, J. H., & Winterer, E. L. Fissure control on volcanic action in the Pacific. In: *Plates, plumes, and paradigms*(eds. Foulger, G. R., Natland, J. H., Presnall, D. C. & Anderson, D. L.) *Geological Society of America Special Paper* **388**, 687-710 (Geol. Soc. Am., Boulder Colorado, 2005).
4. Gordon, R. G., Cox, A. & Harter, C. E. Absolute motion of an individual plate estimated from its ridge and trench boundaries. *Nature* **274**, 752-755 (1978).
5. Sharp, W. D. & Clague, D. A. 50-Ma Initiation of Hawaiian-Emperor Bend Records Major Change in Pacific Plate Motion. *Science* **313**, 1281-1284 (2006).
6. Tarduno, J. A., et al. The Emperor Seamounts: Southward Motion of the Hawaiian Hotspot Plume in Earth's Mantle. *Science* **301**, 1064-1069 (2003).
7. Steinberger, B., Sutherland, R. & O'Connell, R. J. Prediction of Emperor-Hawaii seamount locations from a revised model of global plate motion and mantle flow. *Nature* **430**, 167-173 (2004).
8. Tarduno, J. A. On the motion of Hawaii and other mantle plumes. *Chemical Geology* **241**, 234-247 (2007).
9. O'Connor, J. M., Steinberger, B., Regelous, M., Koppers, A. A. P., Wijbrans, J. R., Haase, K. M., Stoffers, P., Jokat, W. & Garbe-Schönberg, D. Constraints on past plate and mantle motion from new ages for the Hawaiian-Emperor Seamount Chain. *Geochem. Geophys. Geosyst*. **14** (2013).
10. Whittaker, J. M., Müller, R. D., Leitchenkov, G., Stagg, H., Sdrolias, M., Gaina, C. & Goncharov, A. Major Australian-Antarctic Plate Reorganization at Hawaiian-Emperor Bend Time. *Science* **318**, 83-86 (2007).
11. Tarduno, J., Bunge, H. -P., Sleep, N. & Hansen, U. The Bent Hawaiian-Emperor Hotspot Track: Inheriting the Mantle Wind. *Science* **324**, 50-53 (2009).
12. Horner-Johnson, B. C. & Gordon, R. G. True polar wander since 32 Ma B.P.: A paleomagnetic investigation of the skewness of magnetic anomaly 12r on the Pacific plate. *J. Geophys. Res*. **115**, B09101 (2010).
13. Seton, M., Müller, R. D., Zahirovic, S., Gaina, C., Torsvik, T., Shephard, G., Talsma, A., Gurnis, M., Turner, M., Maus, S. & Chandler M. Global continental and ocean basin reconstructions since 200 Ma. *Earth-Science Reviews* **113**, 212–270 (2012).
14. Wessel, P., Harada, Y. & Kroenke, L. W. Toward a self-consistent, high-resolution absolute plate motion model for the Pacific. *Geochem. Geophys. Geosyst*. **7**, Q03L12 (2006).
15. Kopp, H., Kopp, C., Phipps Morgan, J., Flueh, E. R. & Weinrebe, W. Fossil hot spot-ridge interaction in the Musicians Seamount Province: Geophysical investigations of hot spot volcanism at volcanic elongated ridges. *J. Geophys. Res*. **108**, 2160 (2003).
16. Pringle M. S. Age progressive volcanism in the Musicians Seamounts: A test of the hotspot hypothesis for the Late Cretaceous Pacific. In: *The Mesozoic Pacific: Geology Tectonics and Volcanism* (eds. Pringle, M., Sager, W. & Sliter, W.) *American Geophysics Union Geophys. Monograph* **77**, 187-215 (AGU, Washington D. C., 1993).
17. Royer, J. -Y. & Gordon, R. G. The motion and boundary between the Capricorn and Australian Plates. *Science* **277,** 1268-1274 (1997).
18. Sandwell, D. T., Winterer, E. L., Mammerickx, J., Duncan, R. A., Lynch, M. A., Levitt, D. A. & Johnson C. L. Evidence for diffuse extension of the Pacific plate from Pukapuka ridges and cross-grain gravity lineations. *J. Geophys. Res*. **100**, 15,087-15,099 (1995).
19. Matthews, K. J., Williams, S. E., Whittaker, J. M., Müller, R. D., Seton, M. and Clarke, G. L. Geological and kinematic constraints on Late Cretaceous to mid Eocene plate boundaries in the Southwest Pacific. *Earth-Science Reviews* **140**, 72-107 (2015).

20. Engebretson, D. C., Cox, A. & Gordon, R. G. Relative Motions Between Oceanic Plates of the Pacific Basin. *J. Geophys. Res*. **89**, 10,291-10,310 (1984).
21. Reagan, M. K., McClelland, W. C., Girarda, G., Goff, K. R., Peate, D. W., Ohara, Y. & Stern, R. J. The geology of the southern Mariana fore-arc crust: Implications for the scale of Eocene volcanism in the western Pacific. *Earth Planet. Sci.Lett.* **380**, 41-51 (2013).
22. Meffre, S., Falloon, T. J., Crawford, T. J., Hoernle, K., Hauff, F., Duncan, R. A., Bloomer, S. H. & Wright, D. J. Basalts erupted along the Tongan fore arc during subduction initiation: Evidence from geochronology of dredged rocks from the Tonga fore arc and trench. *Geochem. Geophys. Geosyst*. **13**, Q12003 (2012).
23. Ishizuka, O., Tani, K., Reagan, M. K., Kanayama, K., Umino, S., Harigane, Y., Sakamoto, I., Miyajima, Y., Yuasa, M. & Dunkley, D. J. The timescales of subduction initiation and subsequent evolution of an oceanic island arc. *Earth Planet. Sci. Lett.* **306**, 229-240 (2011).
24. Jicha B. R, Scholl D. W., Singer B. S., Yogodzinski G. M. & Kay S. M. Revised age of Aleutian Island Arc formation implies high rate of magma production. *Geology* **34**, 661-664 (2006).
25. Höfig, T. W., Portnyagin, M., Hoernle, K., Hauff, F., Bogaard, P. vd, & Garbe-Schoenberg, C. D. From birth to death of arc magmatism: The igneous evolution of Komandorsky Islands recorded tectonic changes during 50 Ma of westernmost Aleutian history. Abstract V21C-2742 presented at 2013 Fall Meeting, AGU (2013).
26. Butterworth, N. P, Müller, R. D., Quevedo, L., O'Connor, J. M., Hoernle, K. & Morra, G. Pacific Plate slab pull and intraplate deformation in the early Cenozoic. *Solid Earth* **5**, 757-777 (2014).
27. Forsyth, D. W. & Uyeda, S. On the relative importance of the driving forces of plate motion. *Geophys. J. Roy. Ast. S.* **43**, 163-200 (1975).
28. Ballmer, M. D., Ito, G., Wolfe, C. J. & Solomon, S. C. Double layering of a thermochemical plume in the upper mantle beneath Hawaii. *Earth Planet. Sci.Lett.* **376**, 155-164 (2013).
29. Ballmer, M., van Hunen, J., Ito, G., Bianco, T. & Tackley, P. Intraplate volcanism with complex age-distance patterns: A case for small-scale sublithospheric convection, *Geochem. Geophys. Geosys.* **10,** Q06 015 (2009).
30. Koppers, A. A. P., Staudigel, H., Morgan, J. P. & Duncan, R. A. Nonlinear $^{40}Ar/^{39}Ar$ age systematics along the Gilbert Ridge and Tokelau Seamount Trail and the timing of the Hawaii-Emperor Bend. *Geochem. Geophys. Geosys.* **8,** Q06L13 (2007).
31. Sandwell, D. T. & Smith, W. H. F. Global marine gravity from retracked Geosat and ERS-1 altimetry: Ridge segmentation versus spreading rate. *J. Geophys. Res*. **114**, B01411 (2009).
32. Müller, R. D., Dutkiewicz, A., Seton, M. & Gaina, C. Seawater chemistry driven by supercontinent assembly, break-up and dispersal. *Geology* **41**, 907-910 (2013).

Acknowledgements

F. Jourdan is thanked for very useful comments and suggestions. We thank the captain, crew and members of the scientific party for a successful *RV Sonne* SO 142 (HULA II) Expedition. W. Lustenhouwer and S. Matveev performed the electron microprobe analyses. Financial support was provided by the German Federal Ministry of Education and Research (BMBF), The Netherlands Organisation for Scientific Research (NWO).

Author contributions

J.M.O, P.S. and J.P.M conceived the project, and J.P.M. and J.M.O. wrote the proposal that funded the original seagoing work. J.M.O., K.H., F.H. and J.R.W. designed and performed the experiments and data analysis, while R.D.M, N.P.B., and D.T.S. provided supporting materials. J.M.O., K.H. R.D.M and J.P.M wrote the paper. W.J., P.S. and K.H. provided funding essential for carrying out the project.

Additional Information

Supplementary information is available in the online version of the paper. Reprints and permissions information is available online at www.nature.com/reprints. Correspondence and requests for materials should be addressed to J.M.O.

Competing financial interests

The authors declare no competing financial interests.

Figure 1. Locations of sample sites on the Musicians Volcanic Ridges.
Yellow circles in top panel are for locations of SO142 expedition dredge sites and adjacent numbers are for station numbers (see Supplementary Table 1 for sample information). Sample ages are shown also on high-resolution bathymetric maps in Supplementary Figure 1**.** Base map is marine gravity from radar altimetry at a contour interval of 20 mGal[31]. White numbers are for published ages measured in the 1990s and white boxes are for sample locations[16]. Box around the HEB if for an enlarged map with age information in Supplementary Figure 3.

Figure 2. Examples of high-resolution incremental heating $^{40}Ar/^{39}Ar$ age spectra for the Musicians Volcanic Ridges. Pink lines are $^{40}Ar/^{39}Ar$ ages, and grey lines are K/Ca ratios. The reported $^{40}Ar/^{39}Ar$ age ages are weighted age estimates with errors reported on the 95% confidence level, including 0.3%-0.4% standard deviations in the J- value. All samples where monitored against TCR monitor (28.34 ± 0.014 Ma, 1σ). For complete information see Supplementary Table 2 and Supplementary Figure 2 and Methods and Supplementary Methods.

Figure 3. Evidence that deformation volcanism is related to a depleted upper mantle source. a) Nb/Yb vs TiO_2/Yb discrimination diagram. Fractionation of Ti from Yb by garnet provides a proxy for depth of melting. MORB form a shallow array and basalts with significant residual garnet (i.e. OIB) plot above the array. (see Supplementary Note 7 for details).
(b) Isotopic compositions of Musicians (this study) lavas are age-corrected using ages reported here. Representative island (OIB) groups (in red) from the GEOROC database (htpp://georoc.mpch-mainz.gwdg.de) and field for Pacific N-MORB (in blue) from the PETDB database (http://www.petdb.org) are age corrected to 57 Ma. Additional data sources: Cook-Austral from. Other details as for (a) and Supplementary Note 7.

Figure 4. Reconstruction of plates and plate boundaries around the Pacific Ocean Basin (modified from ref. 13 with paleo-age of the ocean crust modified from ref. 32). Plate boundaries are shown in white; Pacific absolute plate motion velocities are from ref. 26 stage rotations; hotspots are magenta stars and hotspot tracks and shows in dark blue; yellow circles delineate deformation volcanism: A –Aleutian subduction zone, IBM – Izu-Bonin-Marianas subduction zone, IPR –Izanagi-Pacific Ridge, M – Musician seamounts; hotspots: H – Hawaii, G – Gilbert, T – Tokelau, L – Louisville.

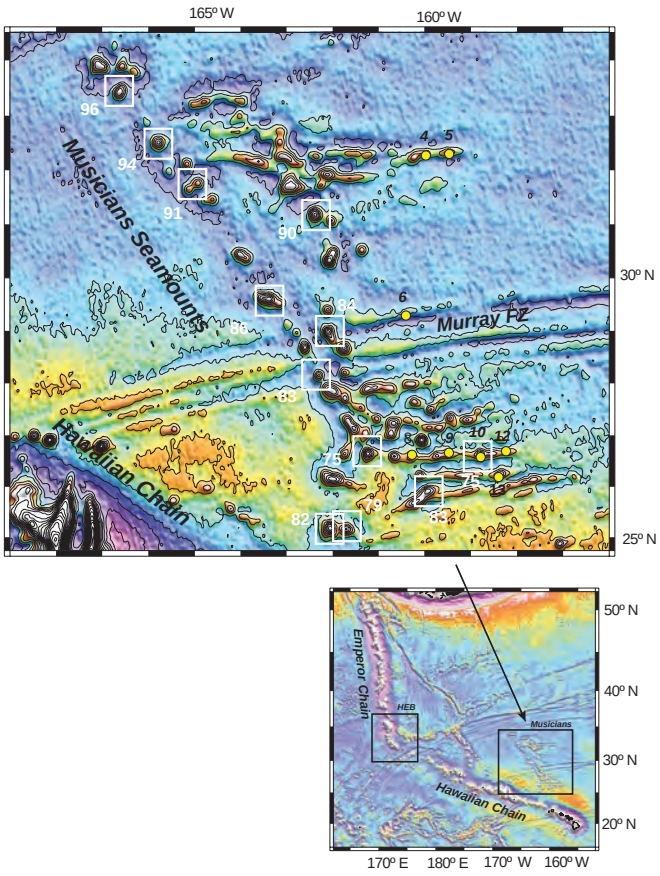
165º W
160º W
30º N
25º N
Musicians Seamounts
Murray Fz
Hawaiian Chain
96
94
91
90
88
83
82
75
6
4
5
10
50º N
40º N
30º N
20º N
170º E
180º E
170º W
160º W
Emperor Chain
HEB
Musicians
Hawaiian Chain

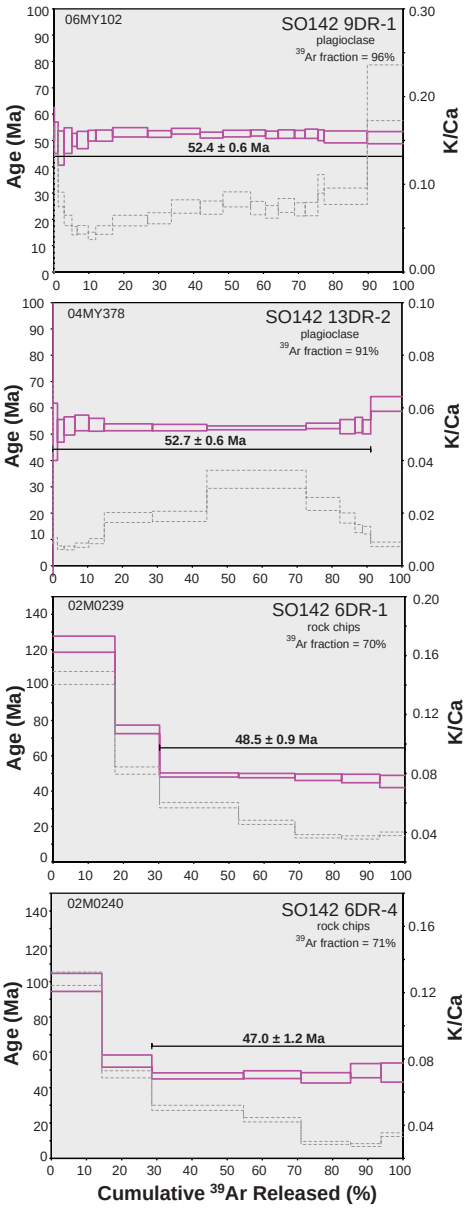

Bach Ridge

Beethoven Ridge

Murray FZ

Murray FZ

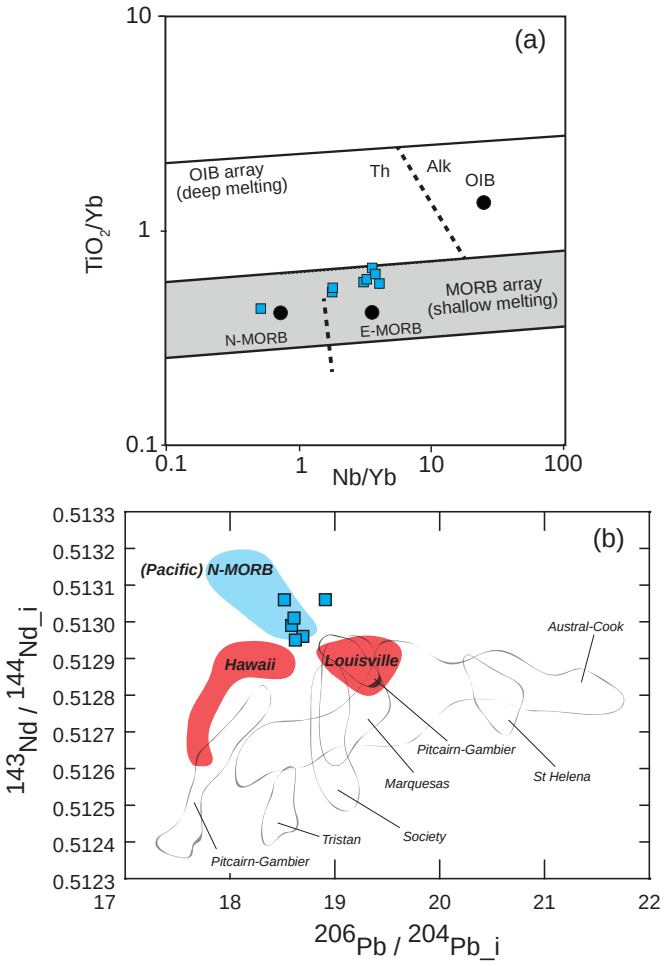
(a)
10
1
0.1
TiO2/Yb
0.1
1
10
100
Nb/Yb
OIB array
(deep melting)
Th
Alk
OIB
MORB array
(shallow melting)
N-MORB
E-MORB
(b)
0.5133
0.5132
0.5131
0.5130
0.5129
0.5128
0.5127
0.5126
0.5125
0.5124
0.5123
143Nd / 144Nd_i
17
18
19
20
21
22
206Pb / 204Pb_i
(Pacific) N-MORB
Hawaii
Louisville
Austral-Cook
Pitcairn-Gambier
Marquesas
St Helena
Tristan
Society
Pitcairn-Gambier

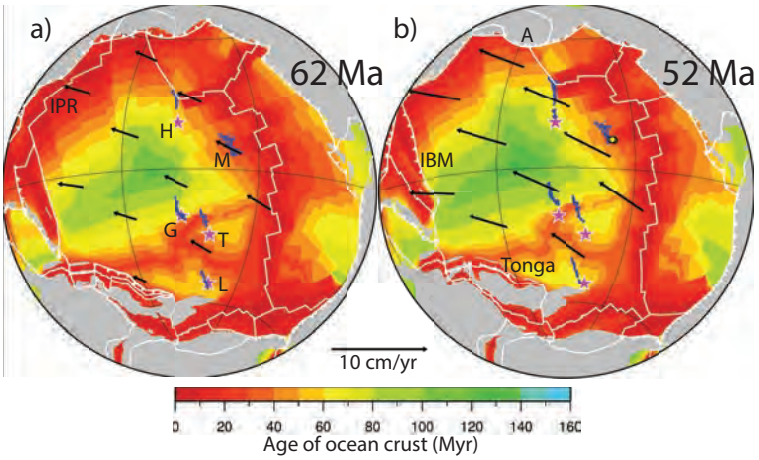
a)
62 Ma
IPR
H
M
G
T
L
b)
52 Ma
A
IBM
Tonga
10 cm/yr
0
20
40
60
80
100
120
140
160
Age of ocean crust (Myr)

SUPPLEMENTARY INFORMATION GUIDE

Deformation-related volcanism in the Pacific Ocean linked to the Hawaiian-Emperor bend

John M. O'Connor[1,2,3], Kaj Hoernle[4], R. Dietmar Müller[5], Jason P. Morgan[6,] Nathaniel P. Butterworth[5], Folkmar Hauff[4], David T. Sandwell[7], Wilfried Jokat[1], Jan R. Wijbrans[3], Peter Stoffers[8]

[1]Alfred Wegener Institute for Polar and Marine Research, Bremerhaven, Germany
[2]GeoZentrum Nordbayern, University Erlangen-Nürnberg, Germany
[3]Faculty of Earth and Life Sciences, VU University Amsterdam, The Netherlands
[4]GEOMAR Helmholtz Centre for Ocean Research Kiel, Germany
[5]EarthByte Group, School of Geosciences, The University of Sydney, New South Wales, Australia
[6] Royal Holloway, University of London, UK
[7]Scripps Institution of Oceanography, La Jolla, California, USA
[8]Institute for Geosciences, Christian-Albrechts-University, Kiel, Germany

Supplementary Dataset 1

Name: Supplementary Information
Format: PDF

Supplementary Methods

Supplementary Notes

Note 1. Paleomagnetic poles
Note 2. Timing of major circum-Pacific plate tectonic events
Note 3. Plate cracking mechanism
Note 4. Classic late stage volcanism
Note 5. Present-day example of deformation-related volcanism.
Note 6. Geologic evidence that subduction forces can cause plate yielding
Note 7. References for Figure 3
Note 8. Explanation of ArArCalc data Excel files

Supplementary Figures

Figure 1. Maps showing sample locations and $^{40}Ar/^{39}Ar$ ages
Figure 2. Incremental heating $^{40}Ar/^{39}Ar$ age spectra
Figure 3. Map of the HEB showing $^{40}Ar/^{39}Ar$ ages
Figure 4. Th/Yb-Nb/Yb and TiO_2/Yb-Nb/Yb discrimination diagrams
Figure 5. Thin section images of rock samples
Figure 6. Back-scattered Electron Detector (BSE) images of mineral separates

Supplementary Tables

Table 1. Sample information
Table 2. $^{40}Ar/^{39}Ar$ incremental heating results
Table 3 XRF, ICM-MS and isotope geochemistry data

Supplementary Dataset 2

Name: Supplementary Excel (ArArCalc) files
Format: Excel

Contents:
ArArCalc output file for each reported $^{40}Ar/^{39}Ar$ age containing complete analytical data and details of age calculations.

Supplementary Methods

ICP-MS geochemistry analyses were carried out at the Institute of Geosciences, University of Kiel using sample preparation and analytical procedures described in refs 33, 34.

Sr, Nd and Pb isotope analyses were carried out at IFM-GEOMAR by thermal ionization mass spectrometry (TIMS), using a Triton and a MAT262 RPQ2+ TIMS, respectively. Sr data are measured on plagioclase mineral separates to avoid problems associated with seawater alteration. Sample preparation and analysis methods are as described in refs 35, 36.

$^{40}Ar/^{39}Ar$ age analyses were carried out at the Laser probe dating facility at the VU University Amsterdam. Data acquisition and reduction, corrections for mass discrimination and age calculation have been described in detail previously[37-39]. Plagioclase size fractions, 250-125 or 74-48 µm, were separated using a combination of heavy liquid and paramagnetic methods. The 250-125 µm fractions were cleaned with 5-8% HF (5 minutes) and 3.5N HCL (60 minutes). Both fractions were cleaned with 1 N HNO_3 (60 minutes) and samples were finally washed with distilled H_2O (60 minutes). All cleaning, except for HF step, was in a 50°C ultrasonic bath water bath. The 500-250 µm whole rock samples were prepared as in ref. 40. Samples were irradiated in the cadmium-shielded CLICIT facility in the TRIGA reactor at Oregon State University and incrementally heated. Ages have been calculated using the Freeware program ArArCalc[41].

Supplementary Fig. 5 contains thin section images of all basalts used for geochemistry and $^{40}Ar/^{39}Ar$ dating. Supplementary Fig. 6 contains Back-Scattered Electron Detector (BSE) compositional maps of plagioclase mineral separates used for $^{40}Ar/^{39}Ar$ dating showing that they are not altered by sericitization[42] or secondary K-feldspar.

The $^{40}Ar/^{39}Ar$ ages reported here meet the following acceptability criteria and thresholds widely used in deciding whether age plateaus are accepted as reliable[16,43-45]:
(a) a well-defined high-temperature age spectrum plateau is created by three or more concordant (within 2σ), contiguous steps representing at least 50% of the ^{39}Ar released,
(b) a well-defined isochron exists for the plateau points, i.e., the mean squares of weighted deviates (MSWD) are not greater than the cut-off value of 2.5, and
(c) the $^{40}Ar/^{36}Ar$ intercepts found by regression analysis are not significantly different from the atmospheric level of 295.5, i.e., the plateau and inverse isochron ages are concordant.

The $^{40}Ar/^{39}Ar$ age data reported in this study have been calculated using ArArCALC v2.5[41]. The Supplementary ArArCalc Excel data files contain the $^{40}Ar/^{39}Ar$ analytical data and isotopic age calculation. Incremental heating $^{40}Ar/^{39}Ar$ age spectra are in Supplementary Fig. 2 and calculated ages are in Supplementary Table 2. The details of the ArArCALC tables and plots are explained in detail in ref. 46 and a summary version is in Supplementary Note 8.

Note 1: Paleomagnetic poles

Discussion of Pacific paleomagnetic poles based on analysis of marine magnetic anomaly skewness data is presented in DiVenere, V. & Kent, D. V. Are the Pacific and Indo-Atlantic hotspots fixed? Testing the plate circuit through Antarctica. *Earth Planet. Sci.Lett.* **170**, 105-117 (1999).

Note 2: **Timing of major circum-Pacific plate tectonic events**

Tectonic events include reorganization of Pacific spreading centres between 55 and 50 Ma[5,10,14], initiation of the Izu-Bonin-Mariana and the Tonga-Kermadec arc systems at ~50-52 Ma[21,22], and evidence from plate reconstructions for far-field tectonic changes such as Australian-Antarctic plate reorganization at 50-53 Ma[10].

Key support:

1) Cessation of spreading in the Tasman Sea. The location of the extinct ridge corresponds to magnetic anomaly 24y, which is about 52.5 my old (using the Gee and Kent 2007 timescale). The date may change slightly depending on the timescale used, but likely not more than +/- 0.5 Ma[47].

2) Whittaker et al. (2007) (ref. 10) demonstrated that a major change in the Australian-Antarctic spreading system occurred between 53 and 50 Ma, starting more or less at the same time when Tasman Sea spreading ceased.

3) Farallon-Pacific fracture zone bends start around chron 24[48] and the direction change and proposed halt of Pacific-Kula plate spreading also starts at chron 24.

4) This is also the time when uplift of the Transantarctic Mountains starts (~55 Ma)[49] *and many other papers.*

5) Cessation of a major accretion phase in the Latest Cretaceous and emplacement of the Okitsu Melange is recorded along Japan due to subduction of hot, buoyant material at 55 Ma[50].

6) Lastly, and perhaps most importantly, there is very solid evidence, summarised in ref. 19 *(*Mattews et al., 2014*)* that subduction initiated around 55 Ma along New Caledonia (see extract below). Tonga subduction initiation is constrained by rocks dredged from the Tonga forearc and trench and yield ages of 52-49 Ma (see extract below). This is slightly younger but the oldest ages are still pretty close to the cessation of spreading in the Tasman Sea (and it would be reasonable to infer a connection between the two events).

Key text from ref. *19 (Mattews et al., 2014)*

"Extensive analysis of rocks from the New Caledonia Peridotite Nappe and underlying obducted ocean floor terranes suggests that there was a subduction initiation event at ~55 Ma to the east of New Caledonia[51-55]. Intrusion of boninitic dykes into the Peridotite Nappe[53] provide evidence for subduction inception[56], as boninites are often associated with the early stages of subduction and high temperatures[e.g. 57]. These boninitic dykes, along with other pre-obduction felsic and mafic dykes with supra-subduction zone affinities that intrude the Peridotite Nappe were interpreted to have formed in a single magmatic event with an average age of ~53 Ma. The ~56 Ma amphibolite lenses found beneath the serpentinite sole of the Peridotite Nappe and above the Poya Terrane formed under high temperature metamorphic conditions slightly earlier than the dyke intrusions[55]. They recrystallised at 850-980°C and 0.5 GPa, at odds with the high pressure-low temperature metamorphic conditions of the eclogite and blueschist facies rocks of the Pouebo and DiahotTerranes[58-60], that are typical of metamorphic rocks associated with subduction, and the largely unmetamorphosed Poya Terrane[55].

This suggested to Cluzel et al. (2012) (ref 55)that subduction inception involved young and warm lithosphere and may have occurred at or near a spreading ridge. Eclogites of the Pouebo Terrane experienced peak metamorphic conditions later, at ~44 Ma[56], on the order of 600°C and 2.4 GPa[59]. The proximal occurrence of abyssal- and supra-subduction peridotites, and contemporaneous ridge and arc volcanism has been proposed as evidence to support the

hypothesis of subduction inception near a spreading ridge[54]. Ulrich et al. (2010) (ref. 54) studied the geochemical trends of the Peridotite Nappe, in particular lherzolites and highly depleted harzburgites from four massifs across New Caledonia and attributed a change in melting style, from dry melting in a ridge environment to hydrous melting in a supra-subduction environment, to a shift from extension to convergence, and specifically subduction inception at or near a spreading ridge. In the models of Ulrich et al. (2010)(ref. 54) and Cluzel et al. (2012) (ref. 55)subduction initiated at the spreading ridge in the South Loyalty Basin, believed to be a back-arc basin that opened to the east of New Caledonia during the Late Cretaceous to Paleocene. In their models changes in plate motion caused compression in the basin and its closure due to subduction.

Tholeiites (back-arc basin-type and island arc-type) dredged from the Tonga forearc and trench that yield ages of 52-49 Ma, have been used to better understand the evolution of the South Loyalty Basin and region to the east of New Caledonia[61]. Formation of these rocks is associated with subduction and is consistent with two alternative scenarios, either they formed in the arc-back-arc transition region of the Loyalty subduction zone discussed by Cluzel et al. (2012) (ref. 55) and this region later became the forearc region of the west-dipping Tonga-Kermadec subduction zone, or alternatively these rocks could have formed in the forearc region of the Tonga-Kermadec subduction zone during incipient subduction[61]".

Note 3: Plate cracking mechanism

Morphologic features in the Crossgrain *en échelon* linear ridges in the Central Pacific indicate that they originate as tension ('pull-apart') cracks in the Pacific plate[2,18,62,63]. In the case of the Musicians Ridges, their very linear trend and elongated volcanic edifices on the top of ridge segments are very similar to the Pukapuka Ridges[15], where such features are explained by tensional plate cracking[18,62] A cracking and shearing mechanism is further suggested by an apparent eastward-stepping, time-progressive, *en échelon* ridge pattern similar to those in the reactivated fracture zones west of the Hawaiian-Emperor Seamount Chain (HESC)[64].

Midplate volcanism may leave the lithosphere more susceptible to the passage of future melts[65]. Such a mechanism could have, for example, thinned the lithosphere, rendering it easier to crack and shear when plate-wide tensional stress increased sufficiently. Moreover, a two-stage mechanism could further explain the perplexing widespread association in the Pacific between chains of volcanic ridges and lineaments in the gravity field[62,63].

Another observation is that the Musicians Ridges merge into the Cretaceous Musicians hotspot trail at their western end and very likely into spreading ridges at their eastern ends[2,15,62]. This implies that late-stage non-hotspot volcanism occurs in linear structures located on lithosphere influenced by earlier Cretaceous hotspot-spreading ridge interaction[15]. Lines of plate weakness such as steps in lithosphere thickness (age) across fracture zones as evidenced by the Musicians Volcanic Ridge in the Murray FZ might have enhanced this mechanism[66-69].

Independent evidence that widespread deformation across the Northwestern Pacific Plate can reactivate pre-existing midplate structures comes from deformation of major fracture zones (Hokkaido, Tuscarora, and Seismikov) located between the HESC and the Kurile Trench, such as vertical displacements of 1000 km-long blocks and along strike *en échelon* ridge offsets[64]. Evidence also exists that midplate volcanism occurs along pre-existing tectonic fabric or around highly stressed lithosphere[3,69,70].

A rapid change in asthenosphere flow associated with subduction initiation could also have helped trigger local upwelling and decompression melting, especially beneath pre-

existing structures such as the Musicians Volcanic Ridges and the Murray fracture zone[65,71-74].

Note 4: Classic late stage volcanism

Late-stage (referred to as rejuvenated or post-erosional) volcanism in many hotspot volcanic chains has more depleted isotopic compositions than the main shield-building stage of volcanism with some having isotopic compositions similar to MORB. Rejuvenated volcanism, however, is highly Si-undersaturated and has enriched, ocean-island-basalt (OIB) type incompatible element abundances (i.e., enrichment in more incompatible, e.g. Th, Nb, Ta and light rare earth, to less incompatible, e.g. Y and heavy rare earth element abundances).

Melts may be present in the low-velocity zone of the uppermost asthenosphere, even in the absence of significant decompression[e.g. 75]. In either case, plate deformation (extension and cracking) along older Cretaceous structures and seafloor would facilitate the rise of asthenospheric melts to the surface.

Note 5: Present-day example of deformation-related volcanism.

The present-day analog for the type of deformation and volcanism that we invoke here for the early Tertiary – the Researcher volcanic ridge and a graben system – is discussed in Roest, W. R. & Collette, B. J. The Fifteen Twenty Fracture Zone and the North American−South American plate boundary. *J. Geol. Soc.* **143**, 833-843 (1986).

Note 6: Geologic evidence that subduction forces can actually cause plate yielding

That the uneven distribution of subduction forces along plate boundaries can induce plate cracking and ultimately even fragmentation was first recognized by ref. 76 (Menard,' *Journal of Geology, 1977, Fragmentation of the Farallon Plate by pivoting subduction*) and has since been confirmed by extensive observations – see especially ref. 77 (Natland and Winterer, *GSA Spec Pap. 2005, Fissure control on volcanic action in the Pacific*).

Furthermore, the breakup of the Nazca into the Cocos and Nazca plates because of different average "*subduction pull-directions*" along the Central American and South America has been a known correlation/pattern since the early 1970s, and this breakup was modeled by some of the earliest regional finite element models that calculated stress distributions in plates induced by plate boundary forces in ref. 78 (Wortel and Cloetingh, *Geology, 1981)* and ref. 79 *(*Wortel and Cloetingh, *AAPG Mem. 1983*).

Note 7: References for Figure 3

Details of Nb/Yb vs TiO_2/Yb discrimination diagram are in Pearce, J. A. Geochemical fingerprinting of oceanic basalts with applications to ophiolite classification and the search for Archean oceanic crust. *Lithos* **100**, 14-48 (2008). Cook-Austral isotope data are from Hofmann, A. W. Chemical differentiation of the earth: The relationship between mantle, continental crust, and oceanic crust. *Earth Planet. Sci. Lett.* **90**, 297- 314 (1988).

Note 8. Explanation of ArArCalc data Excel files (see ref. 46)

Incremental Heating (Data Tables) summary table containing the most important data to calculate the ages and to build the age and K/Ca spectra plots. For each incremental heating

step it lists the ^{36}Ar (in V, from the atmospheric component), ^{37}Ar (in V, from Calcium), ^{38}Ar (in V, from Chlorine), ^{39}Ar (in V, from Potassium), ^{40}Ar (in V, radiogenic Argon), the calculated age (plus 2σ uncertainty), the percent radiogenic ^{40}Ar as recorded in that step, the percent ^{39}Ar (from Potassium) in that step relative to the total amount of ^{39}Ar released in the experiment (a proxy for the step size), and the calculated K/Ca ratio (plus 2σ uncertainty). In the first column the lab analysis number is listed and in the second column the power (in Watts) for the laser used to heat up the sample material. The checkmarks indicate the steps included in the calculations of the plateau age. The results section provides the weighted means for the age plateau in terms of the ^{40}Ar/^{39}Ar ratio, its related age, and the K/Ca ratio. The mean square of weighted deviations (MSWD) and its probability (in %) are given, as well as the total width of the age plateau (in %) and the total number of steps included in the age plateau. The results give an age plateau if the MSWD (dependent on *n*) is smaller than the shown 2σ confidence limit, but if the MSWD is larger, the results are denoted as an error plateau. Finally, the total fusion age is reported, computationally combining all steps (including the steps excluded in the age plateau calculation) into a single fraction (summations are reported below the upper table) and then calculating the ^{40}Ar/^{39}Ar ratio and its related age. The same is done for the K/Ca ratio. The uncertainties on the ages given (directly next to the ages) are internal errors, including the error on the J-value. Analytical errors have these J-value uncertainties subtracted, whereas external errors include uncertainties on the total decay constant.

Age Plateau plot showing the age spectra resulting from the incremental heating with the black horizontal bar indicating the location of the age plateau. All errors shown are 2σ.

K/Ca Plateau plot showing the K/Ca spectra resulting from the incremental heating with the black horizontal bar indicating the location of the age plateau. All errors shown are 2σ.

Normal Isochron plot showing the resulting isochron (pink line) with green squares indicating the points included in the calculation. Blue squares are the excluded data points, while the red circle denotes the location of the total fusion point, which should fall on the isochron if the rock or mineral has remained a closed-system since its eruption and/or crystallization. The black line is the reference line, starting with a ^{40}Ar/^{36}Ar intercept of 295.5 and assuming the plateau age to set its slope. All errors shown are 2σ.

Normal Isochron (Data Tables) summary table listing the ^{39}Ar(k)/^{36}Ar(a) and ^{40}Ar(a+r)/^{36}Ar(a) ratios (plus 2σ uncertainties) used for the normal isochron age calculation, as well as the correlation coefficient (r.i.) that is used in the same calculation and denotes the amount of correlation between the errors in both ratios (with numbers approaching "1" indicating strongly correlated errors). In the first column the lab analysis number is listed and in the second column the power (in Watts) for the laser used to heat up the sample material. The blue checkmarks indicate the steps included in the calculations of the isochron age. The results section lists the ^{40}Ar(r)/^{39}Ar(k) ratio and its related age as derived from the slope of the isochron, as well as the intercept ^{40}Ar(a)/^{36}Ar(a) value, which provides an estimate of the composition of the trapped (initial) argon in the geological material. The statistics section lists computational information about the isochron calculations. The mean square of weighted deviations (MSWD) and its probability (in %) are given. The results give an isochron if the MSWD (dependent on *n*) is smaller than the shown 2σ confidence limit, but if the MSWD is larger, the results are denoted as an error chron. The uncertainties on the ages given (directly next to the ages) are internal errors, including the error on the J-value. Analytical errors have

these J-value uncertainties subtracted, whereas external errors include uncertainties on the total decay constant. By definition the data points selected for the normal isochron are the same as those defining the age plateau, allowing for a direct comparison between the plateau and isochron age calculations.

Inverse Isochron plot showing the resulting isochron (pink line) with green squares indicating the points included in the calculation. Blue squares are the excluded data points, while the red circle denotes the location of the total fusion point, which should fall on the isochron if the rock or mineral has remained a closed-system since its eruption and/or crystallization. The black line is the reference line, starting with a (inverse) $^{40}Ar/^{36}Ar$ intercept of 295.5 on the $^{36}Ar/^{40}Ar$ axis and assuming the plateau age to set the other intercept on the $^{39}Ar/^{40}Ar$

Inverse Isochron (Data Tables) summary table listing the $^{39}Ar(k)/^{40}Ar(a+r)$ and $^{36}Ar(a)/^{40}Ar(a+r)$ ratios (plus 2σ uncertainties) used for the inverse isochron age calculation, as well as the correlation coefficient (r.i.) that is used in the same calculation and denote the amount of correlation between the errors in both ratios (with numbers approaching "0" indicating no correlated errors). In the first column the lab analysis number is listed and in the second column the power (in Watts) for the laser used to heat up the sample material. The blue checkmarks indicate the steps included in the calculations of the isochron age. The results section lists the $^{40}Ar(r)/^{39}Ar(k)$ ratio and its related age as derived from the intercept of the isochron on the $^{39}Ar(k)/^{40}Ar(a+r)$ X-axis, as well as the (inverse) intercept $^{40}Ar(a)/^{36}Ar(a)$ value on the Y-axis, which provides an estimate of the composition of the trapped (initial) argon in the geological material. The statistics section lists computational information about the isochron calculations, including the spreading factor (in %) of the data along the isochron (Jourdan *et al.* 2009). The mean square of weighted deviations (MSWD) and its probability (in %) are given. The results give an isochron if the MSWD (dependent on *n*) is smaller than the shown 2σ confidence limit, but if the MSWD is larger, the results are denoted as an error chron. The uncertainties on the ages given (directly next to the ages) are internal errors, including the error on the J-value. Analytical errors have these J-value uncertainties subtracted, whereas external errors include uncertainties on the total decay constant. By definition the data points selected for the inverse isochron are the same as those defining the age plateau, allowing for a direct comparison between the plateau and isochron age calculations.

References in Supplementary Information

33. Worthington, T. J., Hekinian, R., Stoffers, P., Kuhn, T. & Hauff, F. Osbourn Trough: Structure, geochemistry and implications of a mid-Cretaceous paleospreading ridge in the South Pacific. *Earth Planet. Sci. Lett.* **245**, 685-701 (2006).
34. Garbe-Schönberg, D. Simultaneous determination of 37 trace elements in 28 international rock standards by ICP-MS. *Geostandards Newsletter* **17**, 81-93 (1993).
35. Hoernle, K., et al. Arc-parallel flow in the mantle wedge beneath Costa Rica and Nicaragua. *Nature* **451**, 1094–1098 (2008).
36. Hoernle, K., Hauff, F., van den Bogaard, P., Werner, R., Mortimer, N., Geldmacher, J., Garbe-Schönberg, D. & Davy, B. Age and geochemistry of volcanic rocks from the Hikurangi and Manihiki oceanic Plateaus. *Geochimica et Cosmochimica Acta* **74**, 7196–7219 (2010).
37. Koppers, A. A. P., Staudigel, H. & Wijbrans, J. R. Dating crystalline groundmass separates of altered Cretaceous seamount basalts by the $^{40}Ar/^{39}Ar$ incremental heating technique. *Chemical Geology* **166**, 139-158 (2000).

38. O'Connor, J. M., Stoffers, P. & Wijbrans, J. R. The Foundation Chain: Inferring hotspot-plate interaction from a weak seamount trail. In: *Oceanic Hotspots,* 349-372 (eds. Hekinian, R., Stoffers, P. & Cheminée, J.-L. (Springer-Verlag Berlin Heidelberg New York, 2004).
39. Kuiper, K. F., Deino, A., Hilgen, F. J., Krijgsma, W., Renne, P. R. & Wijbrans, J. R. Synchronizing Rock Clocks of Earth History. *Science* **320**, 500-504 (2008).
40. O'Connor, J. M., Stoffers, P., Wijbrans, J. & Worthington, T., Migration of widespread long-lived volcanism across the Galápagos Volcanic Province: Evidence for a broad hotspot melting anomaly? *Earth Planet Sci. Lett.* **263**, 339–354 (2007).
41. Koppers, A. A. P. ArArCALC – software for $^{40}Ar/^{39}Ar$ age calculations. *Computers Geosciences* **5**, 605–619 (2002).
42. Jourdan, F., Mark, D. F. & Verati, C. Advances in $^{40}Ar/^{39}Ar$ Dating: from Archaeology to Planetary Sciences. *Geological Society, London, Special Publications* **378**, 155 - 174 (2014).
43. Fleck, R. J., Sutter, J. F. & Elliot, D. H. Interpretation of discordant $^{40}Ar/^{39}Ar$ age spectra of Mesozoic tholeiites from Antarctica. *Geochim. Cosmochim. Acta* **41**, 15–32 (1977).
44. Lanphere, M. A. and Dalrymple, G. B. The use of $^{40}Ar/^{39}Ar$ data in evaluation of disturbed K–Ar systems, *Short Papers 4th Int. Conf. Geochronol. Cosmochronol. Isot. Geol.* **78-701**, 241–243 (1978).
45. Dalrymple, G. B., Lanphere, M. A. & Clague D. A. Conventional and $^{40}Ar/^{39}Ar$ ages of volcanic rocks from Ojin (Site 430), Nintoku (Site 432), and Suiko (Site 433) Seamounts and the chronology of volcanic propagation along the Hawaiian–Emperor chain. *Init. Rep. Deep Sea Drill. Proj.* **55**, 659–676 (1980).
46. Koppers, A. A. P., T. Yamazaki, J. Geldmacher, J. S. Gee, N. Pressling, H. Hoshi, *et al*. Limited latitudinal mantle plume motion for the Louisville hotspot. *Nature Geoscience* **5**, 911-917 (2012).
47. Gaina, C., Müller, R. D., Royer, J. Y., Stock, J., Hardebeck, J. & Symonds, P. The tectonic history of the Tasman Sea: a puzzle with 13 pieces. *J. Geophys. Res.* **103**, 12413-12,433 (1998).
48. Caress, D. W., Menard, H. W. & Hey, R. N. Eocene reorganization of the Pacific-Farallon Spreading Center north of the Mendocino Fracture Zone. *J. Geophys. Res.* **93**, 2813-2838 (1988).
49. Stump, E. & Fitzgerald, P. G. Episodic uplift of the Transantarctic Mountains. *Geology* **20**, 161-164 (1992).
50. Agar, S. M., et al. Accretion and uplift in the Shimanto Belt, SW Japan. *Geol. Soc. of London Journal* **146,** 893-896 (1989).
51. Eissen, J. -P., Crawford, A. J., Cotten, J., Meffre, S., Bellon, H. & Delaune, M. Geochemistry and tectonic significance of basalts in the Poya Terrane, New Caledonia. *Tectonophysics* **284**, 203-219 (1998).
52. Cluzel, D., Aitchison, J. C. & Picard, C. Tectonic accretion and underplating of mafic terranes in the Late Eocene intraoceanic fore-arc of New Caledonia (Southwest Pacific): geodynamic implications. *Tectonophysics* **340,** 23-59 (2001).
53. Cluzel, D., Meffre, S., Maurizot, P. & Crawford, A. J. Earliest Eocene (53 Ma) convergence in the Southwest Pacific; evidence from pre-obduction dikes in the ophiolite of New Caledonia. *Terra Nova* **18**, 395-402 (2006).
54. Ulrich, M., Picard, C., Guillot, S., Chauvel, C., Cluzel, D. & Meffre, S. Multiple melting stages and refertilization as indicators for ridge to subduction formation: The New Caledonia ophiolite. *Lithos* **115**, 223-236 (2010).
55. Cluzel, D., Jourdain, F., Meffre, S., Maurizot, P. & Lesimple, S. The metamorphic sole of New Caledonia ophiolite: $^{40}Ar/^{39}Ar$, U-Pb, and geochemical evidence for subduction inception at a spreading ridge. *Tectonics* **31**, TC3016 (2012).
56. Spandler, C., Rubatto, D. & Hermann, R. Late Cretaceous-Tertiary tectonics of the southwest Pacific: insights from U–Pb sensitive, high-resolution ion microprobe (SHRIMP) dating of eclogite facies rocks from New Caledonia. *Tectonics* **24**, TC3003 (2005).
57. Stern, R. J. & Bloomer, S. H.. Subduction zone infancy: examples from the Eocene Izu-Bonin-Mariana and Jurassic California arcs. *Geol. Soc. Am. Bull*. **104**, 1621-1636 (1992).

58. Aitchison, J. C., Clarke, G. L., Meffre, S. & Cluzel, D. Eocene arc-continent collision in New Caledonia and implications for regional southwest Pacific tectonic evolution. *Geology* **23**, 161-164 (1995).
59. Clarke, G. L., Aitchison, J. C. & Cluzel, D. Eclogites and blueschists of the Pam Peninsula, NE New Caledonia: a reappraisal. *J. Pet.* **38**, 843-876 (1997).
60. Fitzherbert, J. A., Clarke, G. L. & Powell, R. Lawsonite–omphacite-bearing metabasites of the Pam Peninsula, NE New Caledonia: evidence for disrupted blueschist-to eclogite-facies conditions. *J. Pet.* **44**, 1805-1831 (2003).
61. Meffre, S., Falloon, T. J., Crawford, T. J., Hoernle, K., Hauff, F., Duncan, R. A., Bloomer, S. H. & Wright, D. J. Basalts erupted along the Tongan fore arc during subduction initiation: Evidence from geochronology of dredged rocks from the Tonga fore arc and trench. *Geochem. Geophys. Geosyst*. **13**, Q12003 (2012).
62. Lynch, M. A. Linear ridge groups: Evidence for tensional cracking in the Pacific plate. *J. Geophys. Res*. **104**, 29,321-29,333 (1999).
63. Sandwell, D. & Fialko, Y. Warping and cracking of the Pacific plate by thermal contraction. *J. Geophys. Res*. **109**, B10411 (2004).
64. Patrikeev, V. N. Deformations of the Northwestern Pacific Plate. *Geotectonics* **47**, 362–375 (2013)
65. Hillier, J. Pacific seamount volcanism in space and time. *Geophs. J. Int*. **168**, 877–889 (2007).
66. McNutt, M., D. Caress, Reynolds, J., Jordahl, K. & Duncan, R. A. Failure of plume theory to explain midplate volcanism in the Southern Austral Islands. *Nature* **389**, 479–482 (1997).
67. Adam, C., Yoshida, M., Isse, T., Suetsugu, D., Fukao, Y. & Barruol, G. South Pacific hotspot swells dynamically supported by mantle flows. *Geophys. Res. Lett.* **37**, L08302 (2010).
68. Kessling, S. Die Tiefenstruktur der Kruste des Discovery Seamounts und des südlichen Walfischrückens im Südatlantik. Diplom thesis, Friedrich Schiller University Jena, Jena (2008).
69. O'Connor, J. M., Jokat, W., le Roex, A., Class, C., Wijbrans, J., Kessling, S., Kuiper, K. & Nebel, O. Hotspot trails in the South Atlantic controlled by plume and plate tectonic processes. *Nature Geoscience*. **5**, 735-738 (2012).
70. Clouard, V. & Gerbault, M. Break-up spots: Could the Pacific open as a consequence of plate kinematics? *Earth Planet. Sci. Lett.* **265,** 195–208 (2008).
71. Phipps Morgan, J., Morgan, W. J. & Price, E. Hotspot melting generates both hotspot volcanism and a hotspot swell. *J. Geophys. Res*. **100**, 8045 (1995).
72. Yamamoto, J., Phipps Morgan, J. & Morgan, W. J. Global plume-fed asthenosphere flow -1: Motivation and model development. *Geological Society of America Special Paper* **430**, 165 (2007).
73. Hieronymus, C. & Bercovici, D. Non-hotspot formation of volcanic chains: Control of tectonic and flexural stresses on magma transport. *Earth Planet. Sci. Lett***. 181**, 539-554 (2000).
74. Anderson, D. Superplumes or supercontinents? *Geology* **22**, 39-42 (1994).
75. Presnall, D. C. & Gudfinnsson, G. H. Oceanic volcanism from the low-velocity zone – without mantle plumes. *J. Pet.* **52**, 1533-1546 (2011).
76. Menard, H. W. Fragmentation of the Farallon Plate by pivoting subduction. *J. Geol*. **86**, 99-110 (1978).
77. Natland, J. H., & Winterer, E. L. Fissure control on volcanic action in the Pacific, In: *Plates, plumes, and paradigms* (eds. Foulger, G. R., Natland, J. H., Presnall, D. C. & Anderson, D.L.) Geological Society of America Special Paper 388, 687-710 (Geol. Soc. Am., Boulder Colorado, 2005).
78. Wortel. R. & Cloetingh, S. On the origin of the Cocos-Nazca spreading center. *Geology* **9**, 425-430 (1981).
79. Wortel, R. & Cloetingh, S. A mechanism for fragmentation of oceanic plates. In: *Continental Margin Geology* (eds. Watkins, J. S. & Drake, C. L.). *Am. Assoc. Pet. Geol*. **34**, 793-801 (1983).
80. Sandwell, D. T. & Smith, W. H. F. Global marine gravity from retracked Geosat and ERS-1 altimetry: Ridge segmentation versus spreading rate *J. Geophys. Res*. **114**, B01411 (2009).

81. Renne, P. R., Swisher, C. C., Karner, D. B., Owens, T. L. & DePaolo, D. J. Intercalibration of standards, absolute ages and uncertainties in $^{40}Ar/^{39}Ar$ dating. *Chem. Geol*. **145**, 117 (1998).
82. Pearce, J. A. Geochemical fingerprinting of oceanic basalts with applications to ophiolite classification and the search for Archean oceanic crust. *Lithos* **100**, 14-48 (2008).
83. Sun, S. -S. & McDonough, W. F. Chemical and isotopic systematics of oceanic basalts: implications for mantle composition and processes. In: *Magmatism in Ocean Basins*, Geological Society Special Publication 42, 313-345. *(*eds. Saunders, A.D., Norry, M.J.) (Geol. Soc. London, 1989).
84. Flueh, E. R., O'Connor, J., Phipps-Morgan, J. & Wagner, J., eds. Cruise report SO142 HULA, Interdisciplinary investigations of the timing of the Hawaii-Emperor Bend and the origin of lithospheric anomalies along the Musician seamount chain, *GEOMAR Report* **90**, ISSN 0936 - 5788, Kiel (1999).
85. Steiger, R. H. & Jager, E. Subcommission on geochronology: Convention on the use of decay constants in geo- and cosmochronology. *Earth Planet Sci. Lett*. **36**, 359-362 (1977).

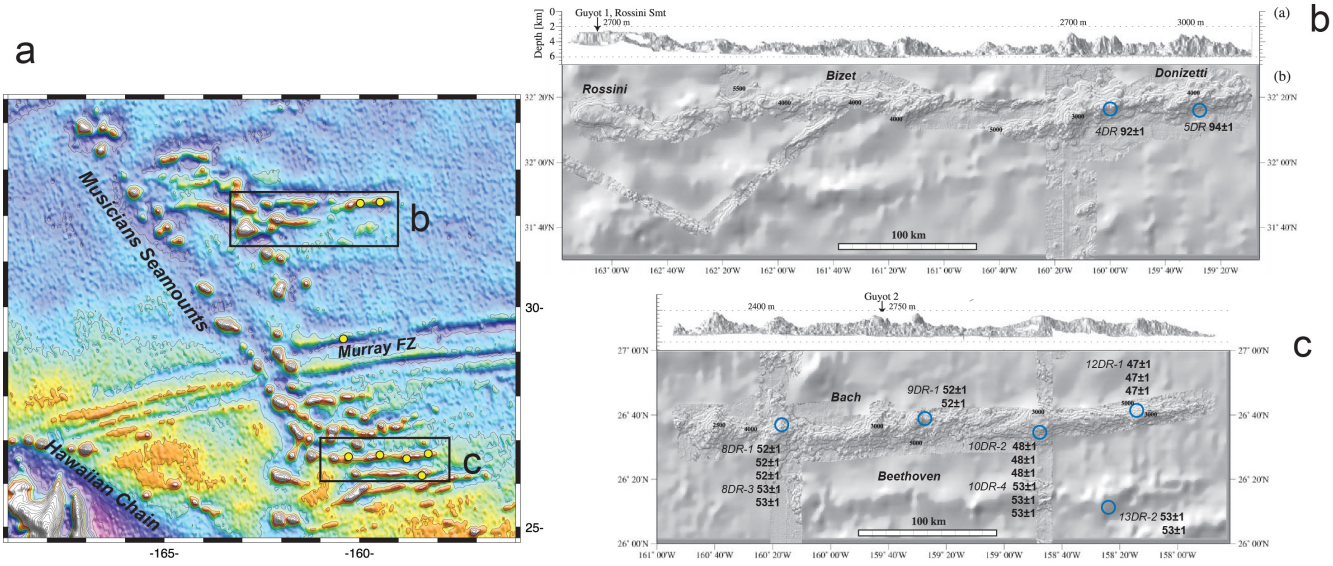

Supplementary Figure 1. Detailed maps of the Musicians Volcanic Ridges showing sample locations and $^{40}Ar/^{39}Ar$ ages. (**a**) Gravity map[80], showing the locations of high resolution bathymetric maps (b & c). Other details as for Fig. 1 in the text. (**b**) High-resolution bathymetric map of the northern and (**c**) southern cluster of Musicians Volcanic Ridges. Blue circles show locations of SO142 expedition dredge-sample sites; adjacent numbers are for dredge sample numbers and measured isotopic ages. Adapted from ref. 15.

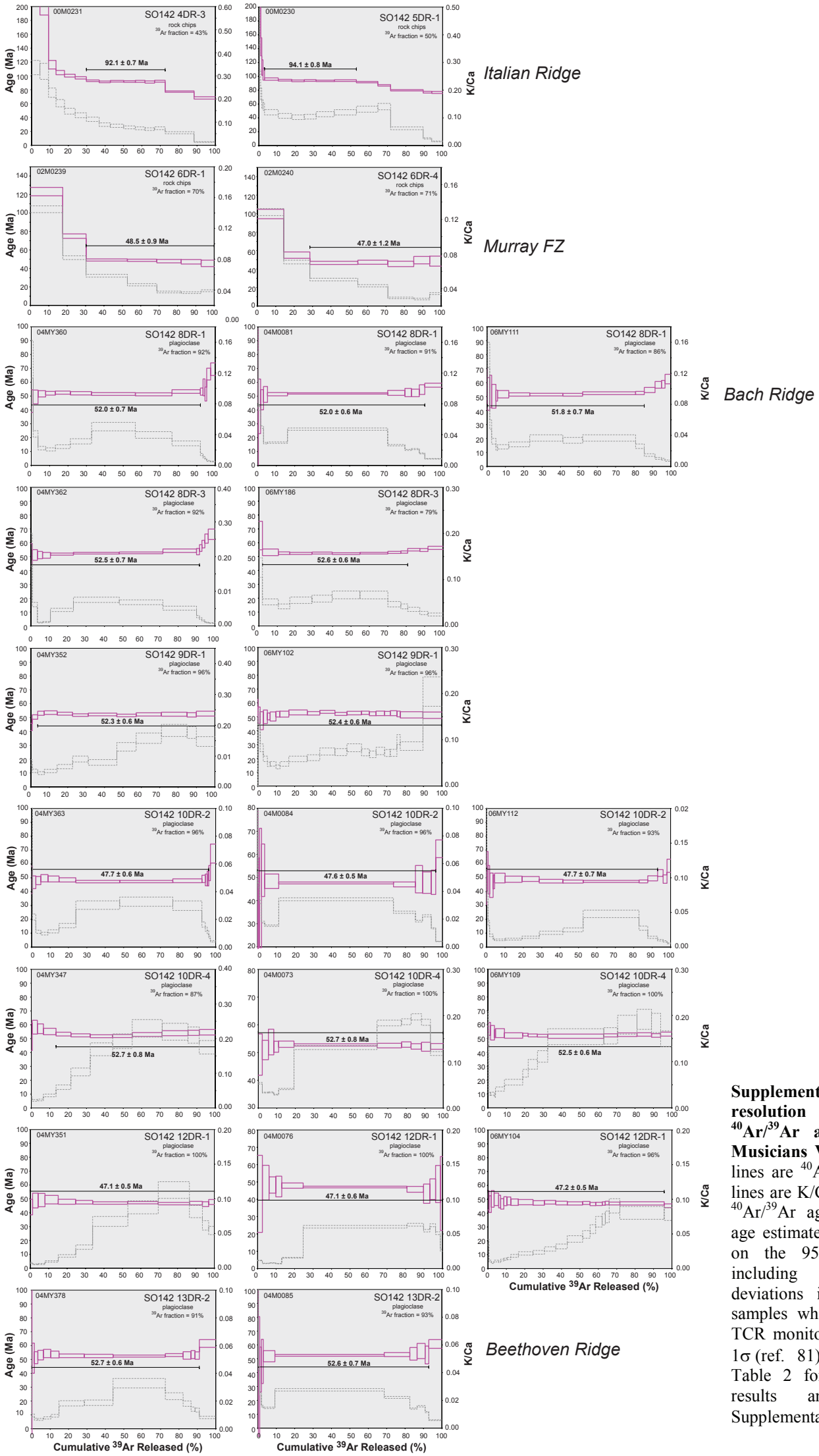

Supplementary Figure 2. High-resolution incremental heating $^{40}Ar/^{39}Ar$ age spectra for the Musicians Volcanic Ridges. Pink lines are $^{40}Ar/^{39}Ar$ ages, and grey lines are K/Ca ratios. The reported $^{40}Ar/^{39}Ar$ age ages are weighted age estimates with errors reported on the 95% confidence level, including 0.3%-0.4% standard deviations in the J- value. All samples where monitored against TCR monitor (28.34 ± 0.014 Ma, 1σ (ref. 81). See Supplementary Table 2 for $^{40}Ar/^{39}Ar$ analytical results and Methods and Supplementary Methods.

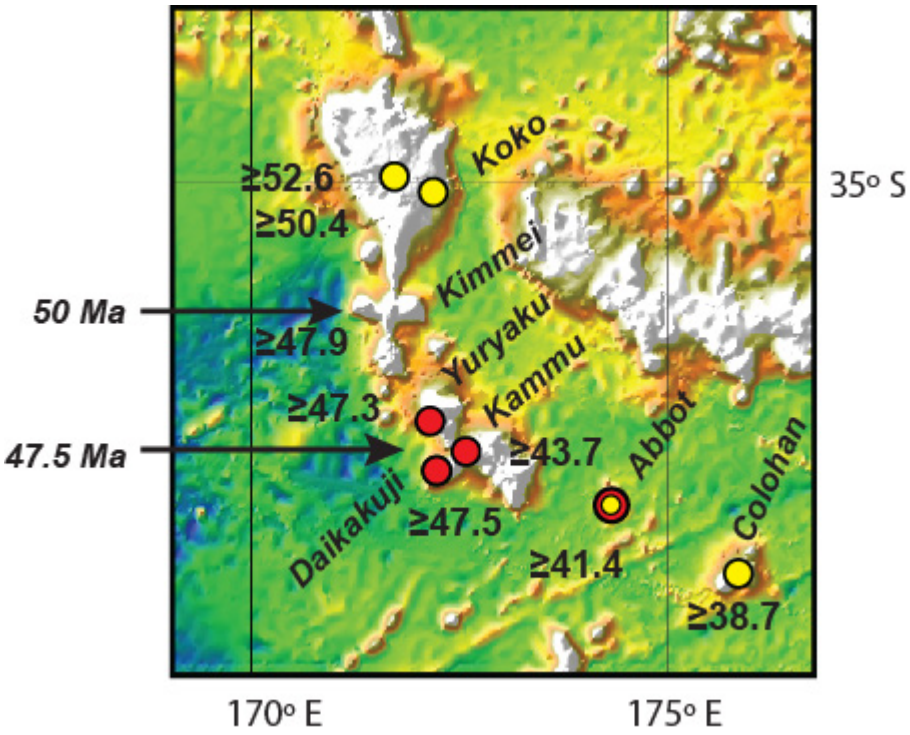

Supplementary Figure 3. Topography map of the HEB adapted from ref. 9. Horizontal arrows are for the interpolated 50 Ma age for the Kimmei Seamount (see refs 5 and 9) and the sharp 47.5 Ma HEB (see ref 9), where the trend of the HESC starts and ends, respectively, rotating from nearly due south to south-easterly. Other numbers are $^{40}Ar/^{39}Ar$ ages in ref. 5 (yellow symbols) and ref. 9 (red symbols).

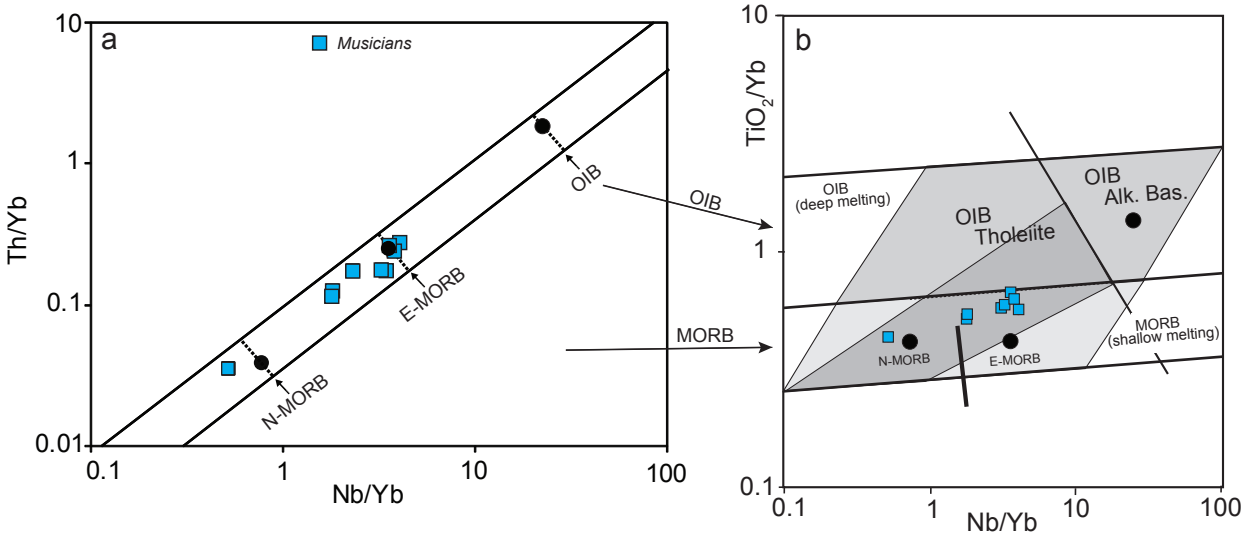

Supplementary Figure 4. Th/Yb-Nb/Yb and TiO2/Yb-Nb/Yb discrimination diagrams[82]. Supporting discrimination diagrams for Figure 3 in the text showing that that Musicians late-stage volcanic rocks have compositions similar to those from mid-ocean-ridge basalts (N-MORB-E-MORB), rather than ocean island basalts (OIB). Solid black dots are for N-MORB, E-MORB and OIB[83]. Dashed lines show boundaries between N-MORB- E-MORB-OIB. Other details as in Figure 3 in the text. (b) utilizes the Ti–Yb proxy for deep melting highlighted. OIB have higher Ti/Yb ratios than MORB reflecting deeper melting resulting from a combination of a thicker lithospheric cap and hotter mantle temperatures. Within OIB, alkalic basalts have the higher Nb/Yb and Ti/Yb ratios. Within MORB, N-MORB lie to the left of the array (defined here as having Nb/Yb <1.45, the C1 chondrite value) and E-MORB to the right of the array (defined here as having Nb/Yb >1.45).

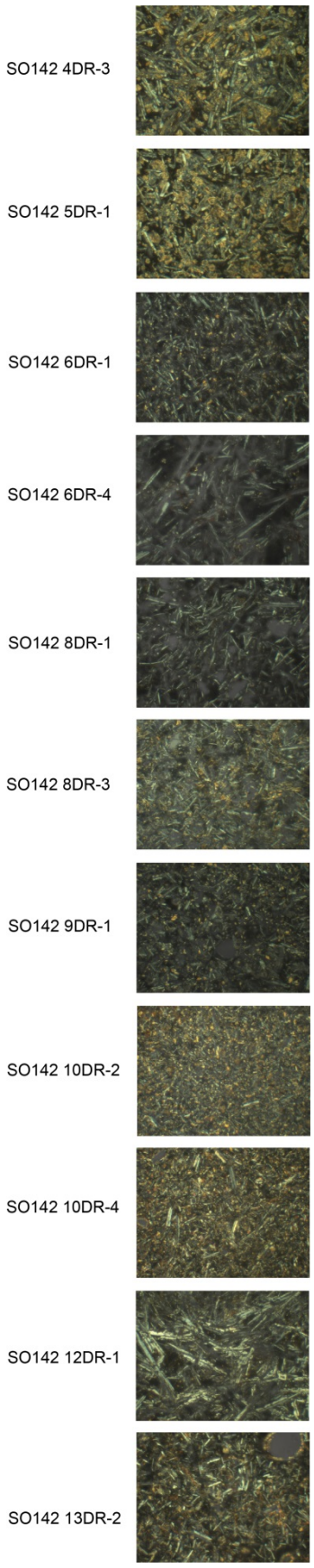

Supplementary Figure 5. Microscopic images of thin-sections of SO142 samples (crossed nicols).

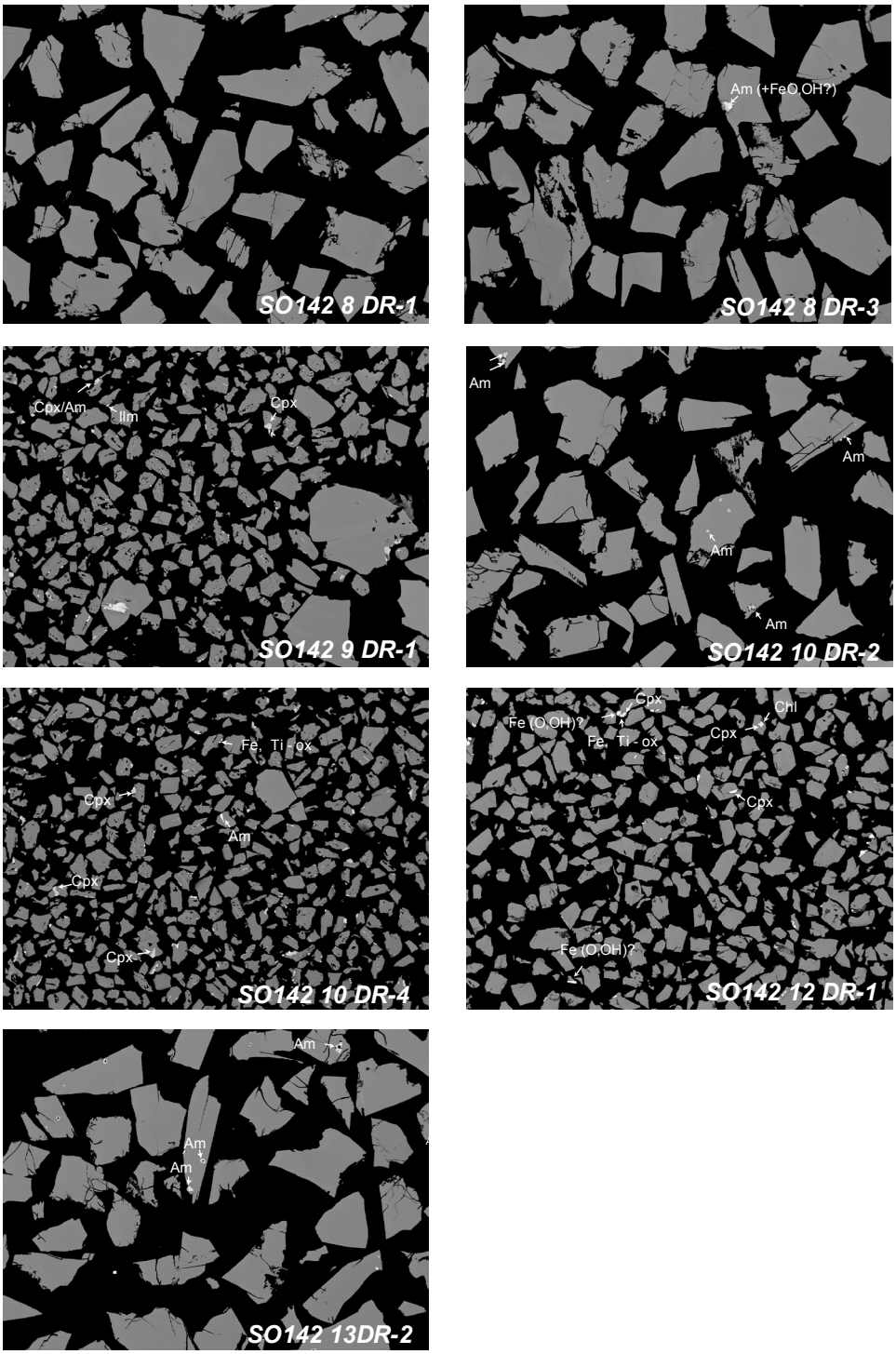

Supplementary Figure 6. Back-scattered Electron Detector (BSE) images showing that acid leached plagioclase mineral separates used for $^{40}Ar/^{39}Ar$ dating were not altered by sericitization or secondary K-feldspar. The number of backscattered electrons (BSE) reaching a BSE detector is proportional to the mean atomic number of the sample, so 'brighter' BSE intensity correlates with greater average Z in the sample, and 'dark' areas have lower average Z. Calculated average atomic numbers (Z): albite (Na) = 10.0; anorthite (Ca) = 10.62; An/Ab 70% = 10.43; K-feldspar = 10.62, and muscovite = 9.43. Spot microprobe analyses show that the plagioclase ranges from An/Ab 50-90%, so the contrast was readily optimised to highlight the presence of K-feldspar in plagioclase, the latter being a darker grey phase. Spot microprobe analyses confirm that any bright areas are not K-feldspar, see examples indicated above. Since the contrast between plagioclase and mica (sericite being near to muscovite) is greater than in the case of K-feldspar, sericite would stand out clearly as a darker phase in the plagioclase groundmass.

Supplementary Table 1. Sample Information

SO142 Expedition information and full station details are ref 84

04 DR **Italian Ridge** *Donizetti Smt*	on bottom: 05:39 5120 m 32°14,99 N 159°56,99 W off bottom: 12:24 3783 m 32°16,54 N 159°58,46 W	-3: Aphyric pillow lava fragment with smoothed edges and moderately altered interior (light grey). Small vesicles (< 1mm) filled with yellowish clay. MnO_x (1.5 cm thick)
05 DR **Italian Ridge** *Donizetti Smt*	on bottom: 16:58 5177 m 32°16.28' N 159°28.02' W off bottom: 21:18 3790 m 32°18.20' N 159°28.19' W	-1: Rounded fragment of moderately altered phyric basalt. Olivine phenocryst (<7%) some altered. Thin (millimetric) MnO_x coating.
06 DR **Murray Ridge** *Fracture Zone*	on bottom: 04:28 5998 m 29°15.51' N 160°24.58' W off bottom: 09:23 5185 m 29°17.56' N 160°24.66' W	-1: Flat slab with laminated texture.The rock has light brown and darker gray horizontal streaks. It could be different cooling unit within a massive flow. Size: 8x11 cm. -4: Subrounded fine grained crystalline basaltic rock with thin MnO_x coating (<1 cm) made up of plagioclase aggregates set in a crystalline groundmass of tiny plagioclase laths and dark mesostasis. Size: 11x10x5 cm.
08 DR **Bach Ridge**	on bottom: 06:24 3996 m 26°37.432' N 160°15.693' W off bottom: 11:25 2964 m 26°36.92' N 160°16.98' W	-1: Highly phyric plagioclase basalt (HPPB) with an altered glassy margin. Aboundant plagioclase (>15%). Some are aggregates probably xenolith. The rock is yellowish light colored. This is a pillow lava fragment. Size: 14x12x11 cm. -3: Highly phyric plagioclase basalt (HPPB) coated with MnO_x (1 cm thick). Plagioclase phyric with relatively fresh groundmass. No preserved glassy margin. Size: 21x14x12 cm.
09 DR **Bach Ridge**	on bottom: 03:47 3931 m 26°39.975' N 159°28.009' W off bottom: 06:50 2855 m 26°39.660' N 159°28.965' W	-1: Angular moderately phyric pillow lava basalt. Few large plagioclase phenocryst (<3%). Patches of MnO_x on the surface. Size: 15x10x15 cm.
10 DR **Bach Ridge**	on bottom: 09:42 4093 m 26°33.81' N 158°47.50' W off bottom: 14:31 3533 m 26°34.66' N 158°47.31' W	-2: Angular porphyristic moderately altered basalt with xenolith inclusions. Also contains large empty cavities. Coated with thin Mn film. Size: 30x23x18 cm. -4: Moderately fresh aphyric angular basaltic fragment coated with MnO_x crust (up to 4 cm thick). No glass seen, fair amount (~10%) of small vesicles occur. Size: 15x8x8 cm.
12 DR **Bach Ridge**	on bottom: 11:53 4466 m 26°42.34' N 158°14.64' W off bottom: 15:50 3643 m 26°41.64' N 158°14.11' W	-1: Subrounded moderately altered basaltic fragment; vesicles and cavities, comprising about 10 –15 % of the rock are filled with rusty colored Fe-hydroxide material. No phenocrysts seen, light gray-green groundmass. Thin MnO_x and pelagic sediment coating. Size 9 x 10 x 5 cm.
13 DR **Beethoven Ridge**	on bottom: 22:08 4905 m 26°09.81' N 158°25.00' W off bottom: 02:47 3765 m 26°11.55' N 158°23.98' W	-2: Large xenolith bearing pillow lava fragment with altered chilled margins. Rusty brown palagonite rim. Maybe some preserved glass. The interior appears fresher with dark gray matrix. Some of the inclusions have angular edges, others are corroded (rounded). Size 50 x 30 x 20 cm.

Supplementary Table 2 $^{40}Ar/^{39}Ar$ analyses of SO142 lavas from the Musicians Ridges

Sample	Lab ID	Micron	Age Spectrum					Total Fusion	Inverse Isochron		
			Age (Ma)	$\%^{39}Ar$	K/Ca	MSWD[a]	n^b	Age (Ma)	Age (Ma)	$^{40}Ar/^{36}Ar$	MSWD[a]
Musicians Linear Ridges, North Pacific											
	Italian Ridge										
Donizetti Seamount											
4-3	00M0231	500-250[c]	92.1 ± 0.7	43	0.08	1.0	7	92.0± 0.7	91.1 ± 1.4	398 ± 114	0.4
5-1	00M0230	500-250[c]	94.1 ± 0.8	50	0.01	1.7	6	92.0± 0.7	93.7 ± 0.8	322 ± 19	0.2
	Murray Ridge (FZ)										
6-1	02M0239	500-250[c]	48.5 ± 0.9	70	0.04	1.5	5	65.0± 1.1	47.0 ± 1.6	306 ± 10	0.5
6-4	02M0240	500-250[c]	47.0 ± 1.2	71	0.03	0.8	5	55.9± 1.3	47.7 ± 2.7	292 ± 16	1.0
	Bach Ridge										
8-1	04MY360	[1]250-125	52.0 ± 0.7	92	0.03	1.3	9	52.6 ± 0.6	52.1 ± 0.7	289 ± 11	1.2
8-1	04M0081	[1]250-125	52.0 ± 0.6	91	0.02	0.7	10	52.5 ± 0.7	52.2 ± 0.6	289 ±10	0.5
8-1	06MY111	[1]250-125	51.8 ± 0.7	86	0.03	0.6	10	52.7 ± 0.7	51.8 ± 0.7	295 ± 6	0.7
8-3	04MY362	[1]250-125	52.5 ± 0.7	92	0.01	2.1	9	53.5 ± 0.6	52.5 ± 0.7	292 ± 16	2.4
8-3	06MY186	[1]250-125	52.6 ± 0.6	79	0.05	1.0	8	53.4 ± 0.6	52.6 ± 0.7	296 ± 11	1.2
9-1	04MY352	[2]74-48	52.3 ± 0.6	96	0.07	1.2	10	52.3 ± 0.6	52.0 ± 0.8	308 ± 21	1.2
9-1	06MY102	[2]74-48	52.4 ± 0.6	100	0.06	1.0	21	52.5 ± 0.7	53.1 ± 0.9	289 ± 6	0.8
10-2	04MY363	[1]250-150	47.7 ± 0.6	96	0.01	0.9	12	48.4 ± 0.6	47.7 ± 0.7	298 ± 13	0.9
10-2	04M0084	[1]250-150	47.6 ± 0.5	96	0.02	0.5	10	48.2 ± 0.8	47.5 ± 0.6	301 ± 16	0.5
10-2	06MY112	[1]250-150	47.7 ± 0.7	93	0.02	1.1	13	48.4 ± 0.7	47.7 ± 0.7	297 ± 6	1.2
10-4	04MY347	[2]74-48	52.7 ± 0.8	87	0.11	2.1	8	53.5 ± 0.7	51.4 ± 3.0	337 ± 69	0.04
10-4	04M0073	[2]74-48	52.6 ± 0.5	100	0.04	0.5	11	52.5 ± 0.6	52.8 ± 0.6	290 ± 11	0.5
10-4	06MY109	[2]74-48	52.5 ± 0.6	100	0.04	0.8	14	52.4 ± 0.8	51.9 ± 1.0	303 ± 8	0.5
12-1	04MY351	[2]74-48	47.1 ± 0.5	100	0.01	0.9	11	47.4 ± 0.6	47.0 ± 0.7	301 ± 28	0.9
12-1	04M0076	[2]74-48	47.1 ± 0.6	100	0.01	0.7	11	46.9 ± 1.0	47.0 ± 0.6	302 ± 21	0.7
12-1	06MY104	[2]74-48	47.2 ± 0.6	96	0.01	0.5	21	47.4 ± 0.7	46.8 ± 0.7	306 ± 13	0.4
	Beethoven Ridge										
13-2	04MY378	[1]250-150	52.7 ± 0.6	91	0.01	0.3	13	53.5 ± 0.6	52.8 ± 0.7	295 ± 7	0.4
13-2	04M0085	[1]250-150	52.6 ± 0.7	93	0.02	0.6	9	53.1 ± 1.0	53.2 ± 1.0	284 ± 13	0.2

Ages are calculated using TCR monitor age of 28.34 ± 0.014 Ma, 1σ)[81] and decay constant of λ = 5.543 x 10^{-10}/yr[85]
$^{40}Ar/^{39}Ar$ ages were measured using the argon laser probe at VU University Amsterdam.
Measured ages have been calculated using the Freeware software ArArCALC[41]
ArArCALC data are available as Supplementary Excel files. See supplementary information for explanation of ArArCALC files.
Correction factors:
$^{40}Ar/^{39}Ar$ (K) = 0.00086
$^{36}Ar/^{37}Ar$ (Ca) = 0.00026
$^{39}Ar/^{37}Ar$ (Ca) = 0.00067
[a]MSWD values for the age plateaus and inverse isochrons are calculated using N-1 and N-2 degrees of freedom, respectively.
[b]n is for the number of included heating steps.
[d]rock chips, see sample preparation details in[40]
[1]3.5N HCL (60 minutes), 5-8% HF (5 minutes); 1 N HNO_3 (60 minutes); [2]1 N HNO_3 (60 minutes)

Supplementary Table 3. XRF, ICP-MS and Isotope data

Cruise	***SO 142***	***SO 142***	***SO 142***	***SO 142***	***SO 142***	***SO 142***	***SO 142***	***SO 142***	***SO 142***	***SO 142***	***SO 142***
Sample ID	***DR 5-1***	***DR 8-1***	***DR 8-3***	***DR 9-1***	***DR 10-2***	***DR 10-4***	***DR 12-1***	***DR 13-2***	***DR 13-2****	***DR 6-1***	***DR 6-4***
AGE(Ma)		52.0	52.5	52.0	47.5	52.5	47.0	52.5			
Li	87.8	13.8	10.8	12.4	25.1	7.335	48.8	32.8			
Sc	36.8	43.7	45.2	45.5	49.4	52.6	46.3	40.6			
V	263	202	226	276	322	296	277	303			
Co	46.3	33.9	40.7	38.5	51.9	44.8	54.4	37.5			
Cu	162	195	99	120	104	103	186	78.9			
Zn	371	129	113	138	108	95	270	175			
Ga	19.2	20.5	19.2	21.2	18.8	18.6	17.6	20.2			
Rb	17.8	22.1	23.1	31.7	43.5	22.0	12.9	19.7			
Sr	224	237	210	254	250	269	160	272			
Y	40.2	31.1	29.8	39.0	34.9	32.8	29.9	35.7			
Zr	189	99	92	158	129	121	72.8	151			
Nb	14.1	5.076	4.91	11.501	9.96	8.81	1.39	11.7			
Cs	1.04	0.84	0.860	1.108	5.28	0.521	0.898	1.45			
Ba	94.0	57.5	38.2	69.8	56.9	70.6	15.8	60.1			
La	14.1	5.3	5.5	11.8	10.8	9.18	4.74	10.5			
Ce	28.4	12.7	12.6	24.5	20.4	18.4	7.80	23.5			
Pr	4.37	2.07	2.03	3.72	3.48	3.03	1.67	3.53			
Nd	20.5	10.6	10.5	17.8	16.5	14.6	8.87	16.7			
Sm	5.42	3.40	3.33	5.12	4.50	4.03	2.88	4.66			
Eu	1.85	1.31	1.28	1.81	1.61	1.48	1.13	1.66			
Gd	6.24	4.33	4.21	6.07	5.36	4.87	3.88	5.44			
Tb	1.05	0.777	0.755	1.03	0.911	0.833	0.713	0.940			
Dy	6.57	5.12	4.94	6.44	5.83	5.34	4.75	5.86			
Ho	1.35	1.07	1.03	1.30	1.20	1.10	1.01	1.20			
Er	3.69	2.93	2.83	3.49	3.25	3.011	2.80	3.28			
Tm	0.543	0.439	0.419	0.504	0.478	0.442	0.417	0.483			
Yb	3.55	2.89	2.77	3.28	3.11	2.89	2.73	3.16			
Lu	0.529	0.427	0.404	0.480	0.454	0.434	0.405	0.470			
Hf	4.17	2.52	2.45	3.75	3.06	2.91	1.91	3.51			
Ta	0.837	0.317	0.314	0.701	0.610	0.544	0.097	0.708			
Pb	1.00	2.358	0.438	0.756	0.738	0.653	0.440	0.736			
Th	1.00	0.339	0.356	0.880	0.563	0.517	0.099	0.780			
U	0.539	0.436	0.287	0.496	0.275	0.262	0.256	0.293			
87Sr/86Sr		0.703415	0.703262	0.703396	0.703823	0.703216	0.703009	0.703104	0.703070		
87Rb/86Sr		0.270	0.319	0.361	0.504	0.237	0.234	0.209	0.209		
87Sr/86Sr_i		0.703216	0.703024	0.703130	0.703483	0.703039	0.702853	0.702948	0.702914		
143Nd/144Nd		0.513128	0.513127	0.513024	0.513000	0.513042	0.513042	0.513067	0.513061		
ENd		9.56	9.53	7.52	7.06	7.89	7.89	8.37	8.25		
147Sm/144Nd		0.194	0.191	0.173	0.164	0.166	0.195	0.168	0.168		
143Nd/144Nd_i		0.513062	0.513061	0.512965	0.512949	0.512985	0.512982	0.513009	0.513003		
ENd_i		9.58	9.57	7.68	7.26	8.09	7.90	8.56	8.44		
206Pb/204Pb		18.9975	18.8460	19.0220	18.7856	18.7822	18.7292	18.8047	18.7989		
207Pb/204Pb		15.5430	15.5376	15.5791	15.5385	15.5386	15.5496	15.5398	15.5379		
208Pb/204Pb		38.2562	38.2506	38.6436	38.3748	38.3500	38.1738	38.4411	38.4274		
238U/204Pb		11.79	41.73	42.11	23.78	25.55	36.91	25.44	25.43		
232Th/204Pb		9.47	53.47	77.10	50.24	52.11	14.81	69.83	69.81		
206Pb/204Pb_i		18.9020	18.5048	18.6809	18.6097	18.5732	18.4591	18.5967	18.5909		
207Pb/204Pb_i		15.5385	15.5215	15.5630	15.5302	15.5288	15.5369	15.5300	15.5281		
208Pb/204Pb_i		38.2319	38.1116	38.4450	38.2566	38.2145	38.1393	38.2595	38.2458		

* Replicate Analyses

SiO2	47.38	48.10	49.17	48.12	49.64	49.43	46.44	48.01		47.15	46.10
Al2O3	16.21	20.65	19.16	15.99	16.06	16.20	17.91	17.83		15.34	15.72
Fe2O3	9.53	10.17	9.22	12.41	9.94	10.86	11.91	10.54		15.06	15.11
MnO	0.14	0.13	0.13	0.15	0.13	0.17	0.16	0.13		0.17	0.12
MgO	6.36	1.92	2.99	3.59	5.20	4.58	4.61	3.86		3.44	2.61
CaO	8.00	10.28	10.87	9.40	11.07	11.28	10.26	10.99		8.54	8.61
Na2O	3.30	2.67	2.63	2.66	2.97	2.80	2.65	2.84		2.83	2.77
K2O	0.91	1.08	1.15	1.46	0.72	1.14	0.58	0.79		0.88	0.91
TiO2	2.05	1.53	1.52	2.25	1.89	1.71	1.21	2.03		2.73	2.68
P2O5	0.34	0.39	0.31	0.64	0.23	0.29	0.15	0.39		0.26	0.69
SO3	0.00	0.01	0.00	0.02	0.00	0.00	0.00	0.00		0.01	0.02
L.O.I	5.40	3.45	2.59	3.40	2.21	1.55	4.21	2.95		3.88	4.71
SUM	99.62	100.38	99.74	100.09	100.06	100.01	100.09	100.36		100.29	100.05